Kovove Mater. 59 2021 79–91
DOI: 10.4149/km_2021_2_79

Effect of heat treatments on microstructure and mechanical properties of $Al_{0.5}CoCrFeNi$ complex concentrated alloy

J. Lapin[1]*, M. Makwana[1,2], A. Klimová[1]

[1] *Institute of Materials and Machine Mechanics, Slovak Academy of Sciences, Dúbravská cesta 9, 845 13 Bratislava, Slovak Republic*
[2] *Slovak University of Technology in Bratislava, Paulínska 16, 917 24 Trnava, Slovak Republic*

Received 11 March 2021, received in revised form 26 April 2021, accepted 30 April 2021

Abstract

The effect of heat treatments on microstructure and mechanical properties of $Al_{0.5}CoCrFeNi$ complex concentrated alloy (CCA) was studied. The CCA was prepared by vacuum induction melting of pure elements and solidification in ceramic crucibles. The as-solidified alloy was subjected to heat treatments consisting of solid solution annealing, water quenching and precipitation hardening. The microstructure of the as-solidified alloy consists of fcc(A1) dendrites and an interdendritic region composed of bcc(B2), bcc(A2) and fcc(A1) phases. The solution annealing followed by water quenching and ageing at 800 and 900 °C leads to the precipitation of needle-like bcc(B2) particles in fcc(A1) dendrites and the formation of the interdendritic region composed of bcc(B2) and fcc(A1) phases. The volume fraction of needle-like bcc(B2) precipitates increases with increasing ageing time and decreasing ageing temperature. The size of bcc(B2) precipitates increases with increasing ageing time and ageing temperature. Vickers microhardness, Vickers hardness and room temperature yield strength of the heat-treated alloy increase with decreasing ageing temperature and increasing ageing time up to 5 h and then decrease at a longer ageing time up to 25 h.

K e y w o r d s: complex concentrated alloys, precipitation hardening, heat treatment, microstructure, mechanical properties

1. Introduction

Multi-principal element alloys (MPEA) with chemical compositions located in the central regions of the multicomponent phase diagram, including high entropy alloys (HEAs) and complex concentrated alloys (CCAs), attract significant research interests [1–5]. HEAs contain at least five or more principal elements stabilized in a single-phase disordered solid solution by their high configuration entropy [1, 6–9]. However, a single-phase microstructure severely limits the performance of HEAs in real-world engineering applications. The CCAs with multi-principal elements preserve the "high entropy" nature of the parent matrix and add complex precipitates as strengtheners [1, 2, 10, 11]. Among numerous CCAs [2], $Al_xCoCrFeNi$ is a prominent system with a microstructure changing from fcc(A1) (face-centred cubic crystal structure A1) to bcc(A2) (body-centred cubic crystal structure A2) with increasing Al content from $x = 0$ to 2 (in molar ratio). Depending on the content of Al and applied processing routes, $Al_xCoCrFeNi$ alloys display a wide spectrum of microstructures and mechanical properties [12–17]. Joseph et al. [12] and Shun and Du [18] have reported for $Al_{0.3}CoCrFeNi$ alloy with fcc(A1) structure a low yield strength, moderate work hardening rate and excellent ductility at room temperature. On the other hand, $Al_{0.875}CoCrFeNi$ alloy composed of disordered bcc(A2), ordered bcc(B2) (body-centred cubic crystal structure B2) and fcc(A1) phases showed exceptionally high yield strength, good plastic deformation in compression but no tensile ductility at room temperature [16]. While low yield strength, low strain hardening rate and high plasticity at room temperature are beneficial to some cold working processes (e.g. cold rolling), high strength is required for high-

*Corresponding author: e-mail address: juraj.lapin@savba.sk

-temperature structural applications of CCAs. Hence, Al_xCoCrFeNi alloys based on fcc(A1), which can be reinforced with bcc(A2)/bcc(B2) precipitates through appropriate heat treatments, can meet an appropriate combination of properties required for their manufacturing processes and applications. Despite the previous works on CCAs, only limited information has been reported on heat treatments, precipitation hardening and mechanical properties of $Al_{0.5}$CoCrFeNi alloy. Besides, contradictory informations on phase transformation temperatures and phase equilibria have been reported by several authors [19–23] for this system.

The present work aims to study the effect of heat treatments on microstructure and mechanical properties of $Al_{0.5}$CoCrFeNi complex concentrated alloy (CCA). The alloy was prepared by vacuum induction melting of pure elements and solidification in ceramic crucibles. The experimental results on solidification, solid solution annealing, water quenching, precipitation hardening, and room temperature mechanical behaviour are reported and discussed.

2. Experimental procedure

The studied $Al_{0.5}$CoCrFeNi alloy was prepared by vacuum induction melting from master binary Ni-50Cr (at.%) and Fe-50Co (at.%) alloys in a medium frequency induction furnace. The charge consisting of master alloys and pieces of pure Al (purity 99.995 %) was induction melted in a conical Al_2O_3 crucible (purity 99 %) with a minimum outside diameter of 35 mm, a maximum outside diameter of 45 mm, a wall thickness of 2.5 mm and height of 95 mm. Before melting, the vacuum chamber of the induction furnace was evacuated to a vacuum pressure of 4.8 Pa, flushed with argon three times and finally partially filled with argon (purity of 99.9995 %) to a vacuum pressure of 10 kPa to minimize evaporation loss of Al during melting [24–26]. The charge was heated to a melt temperature of 1600 ℃ and held at this temperature for 4 min to achieve full dissolution of all alloying elements. The temperature of the melt was measured by a pyrometer. The solidification of the melt was carried out in the ceramic crucible by switching off the induction heating of the furnace [27]. The as-solidified conical sample with a minimum diameter of 30 mm, a maximum diameter of 33 mm and a length of 51 mm was cut to smaller pieces and subjected to heat treatments.

The heat treatments consisted of solution annealing at three temperatures, water quenching and ageing at two temperatures. The solution annealing at 1280 ℃ was performed for 8 h on the as-solidified samples under flowing high-purity argon. The solution annealing at 1330 and 1360 ℃ for 1 h was carried out on the samples subjected to prior solution annealing at 1280 ℃ for 8 h. Each solution annealed sample was quenched into the water with a temperature of 20 ℃. The ageing at 800 and 900 ℃ for various time ranging from 2 to 25 h in the air was carried on the water quenched samples subjected to solution annealing at 1280 ℃ for 8 h.

Vickers microhardness HV_m was measured on polished and slightly etched samples under a load of 0.49 N and loading time of 10 s. Average microhardness values were calculated from 20 independent measurements carried out for each analyzed sample. Vickers hardness HV was performed at an applied load of 98.4 N and loading time of 10 s. Average hardness values were calculated from 10 independent measurements carried out for each analyzed sample. Compression specimens with a diameter of 5 mm and length of 7.5 mm were prepared by lathe machining from heat-treated samples. The surface of the specimens was polished to a roughness better than 0.3 μm. Room temperature compression tests up to a true strain of 0.5 were carried out at an initial strain rate of $10^{-3}\,s^{-1}$ using a Gleeble 3800 thermomechanical tester.

Phase transformation temperatures were determined by differential thermal analysis (DTA) on samples with a diameter of 6 mm and length of 5 mm cut from the as-solidified sample. DTA measurements were performed in Al_2O_3 crucibles under high purity argon (99.995 %) with heating and cooling rates of $10\,℃\,min^{-1}$.

Microstructure evaluation was performed by light microscopy (LM), scanning electron microscopy (SEM), scanning electron microscopy in backscattered electron mode (BSE), energy-dispersive X-ray spectroscopy (EDS), and X-ray diffraction analysis (XRD). Metallographic preparation of the samples consisted of standard grinding using abrasive papers and polishing on diamond pastes with a various grain size up to 0.25 μm. LM samples were electrolytically polished in a solution composed of 66 ml methanol and 33 ml HNO_3 or etched in a reagent of 20 ml HNO_3, 20 ml H_2O, 20 ml HF, and few drops of H_2SO_4. X-ray diffraction (XRD) analysis was carried out by a diffractometer Bruker D8 equipped with an X-ray tube with rotating Cu anode operating at 12 kW. The volume fraction of coexisting phases and size of precipitates were measured by computerized image analysis using digitalized micrographs, and the measured data were treated statistically.

3. Results and discussion

3.1. Chemical and phase composition

Table 1 summarizes the nominal and measured chemical composition of the studied $Al_{0.5}$CoCrFeNi alloy. While the measured average content of Co, Fe, Cr, and Al corresponds to the nominal composition,

Table 1. Nominal and measured chemical composition of the studied $Al_{0.5}CoCrFeNi$ alloy (at.%)

Composition	Co	Cr	Fe	Ni	Al
Nominal	22.2	22.2	22.2	22.2	11.2
Measured	22.1 ± 0.3	22.6 ± 0.3	22.1 ± 0.2	21.8 ± 0.3	11.4 ± 0.3

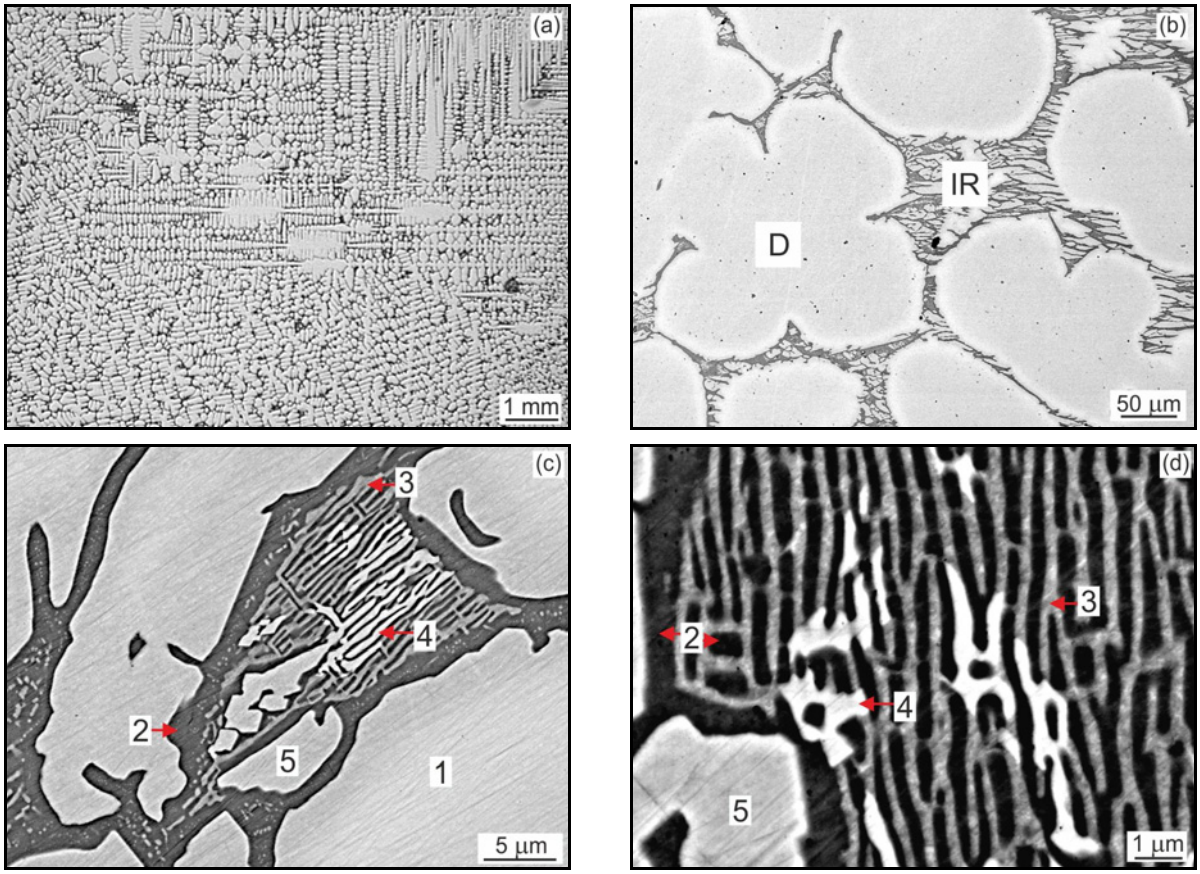

Fig. 1. The typical microstructure of as-solidified $Al_{0.5}CoCrFeNi$ alloy: (a) transversal section of the sample showing the dendritic structure, LM, (b) the morphology of dendrites D, the orientation of secondary dendritic arms and morphology of interdendritic region IR, BSE, (c) BSE micrograph showing multiphase interdendritic region, and (d) detail showing net-like phases formed in the interdendritic region, BSE.

the content of Ni is slightly lower, and Cr is slightly higher than nominal ones. Figure 1 shows the typical dendritic microstructure of the studied alloy formed at non-steady-state growth conditions characterized by a continuous decrease of cooling rate from about 270 to about 60 °C min^{-1} with decreasing sample temperature from 1600 to 1000 °C during solidification in the ceramic crucible [27]. Figure 1a shows the morphology of dendrites (89 vol.%) and orientation of secondary and tertiary dendritic arms on a transversal section of the as-solidified sample. The secondary dendritic arms form the typical "Maltese cross", as seen in Fig. 1b. Figures 1b–d indicate that the interdendritic region marked as IR (11 vol.%) of the as-solidified alloy is composed of three chemically different phases: black coloured matrix (region 2), grey colour phase with net-like morphology (region 3), white colour phase (region 4) with net-like morphology and white colour irregular shaped particles (region 5). Table 2 summarizes the measured average chemical composition of the coexisting phases. The chemical composition of the dendrites marked as D (region 1) is close to those of white colour net-like phase (region 4) and irregularly shaped particles (region 5) formed in the interdendritic region. The black coloured phase (region 2) is enriched in Al and Ni at the expense of Co, Cr, and Fe compared to the average chemical composition of the alloy (Table 1). The grey colour net-like phase (region 3) is enriched by Cr and depleted in Co and Ni.

The XRD pattern of the as-solidified alloy indicates the peaks of three coexisting phases: fcc(A1) (face-centred cubic crystal structure A1, Pearson symbol

Table 2. Phase composition of coexisting phases measured by EDS (at.%)

Region	Phase	Co	Cr	Fe	Ni	Al
1	fcc(A1)	21.0 ± 0.1	24.1 ± 0.2	20.9 ± 0.1	23.4 ± 0.1	10.6 ± 0.3
2	bcc(B2)	16.4 ± 0.2	9.0 ± 0.5	11.4 ± 0.3	32.5 ± 0.6	30.7 ± 0.8
3	bcc(A2)	18.7 ± 0.2	35.5 ± 2.5	20.8 ± 0.8	13.9 ± 1.8	11.0 ± 1.7
4	fcc(A1)	22.5 ± 0.3	24.2 ± 1.0	22.2 ± 0.8	19.5 ± 0.6	11.6 ± 1.5
5	fcc(A1)	22.2 ± 0.2	23.0 ± 0.3	22.2 ± 0.3	22.0 ± 0.4	10.7 ± 0.4

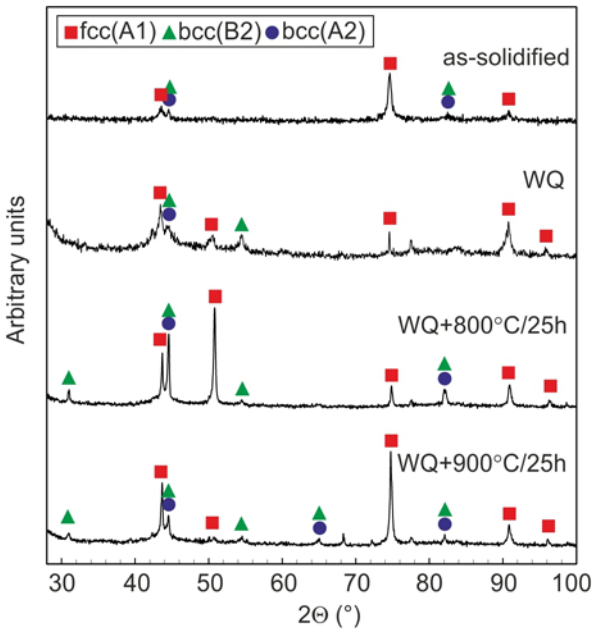

Fig. 2. Examples of XRD patterns of the as-solidified and heat-treated $Al_{0.5}CoCrFeNi$ alloy. The heat treatment consisted of solution annealing at 1280 °C for 8 h, followed by water quenching (WQ) and ageing at 800 and 900 °C for 25 h.

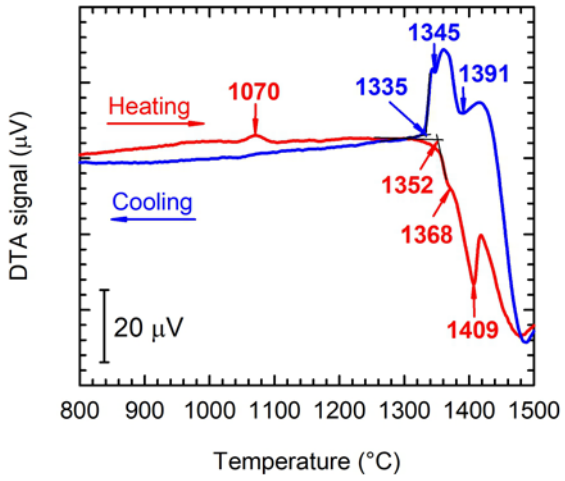

Fig. 3. DTA heating and cooling curves of the studied $Al_{0.5}CoCrFeNi$ alloy.

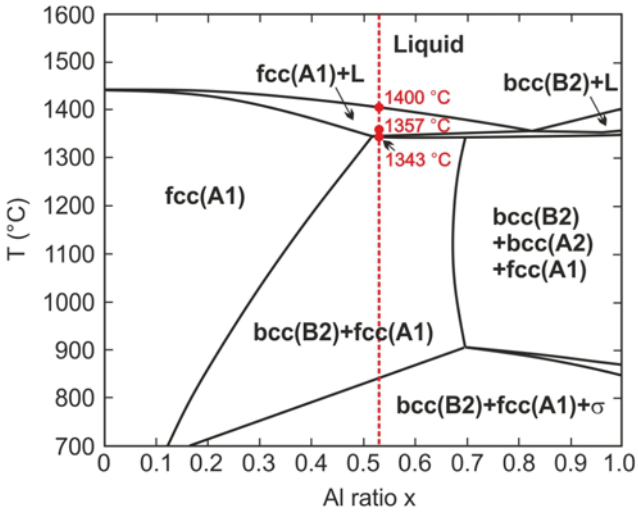

Fig. 4. Calculated isopleth of the $Al_xCoCrFeNi$ alloys [20].

cF4), bcc(A2) (body centred cubic crystal structure A2, Pearson symbol cI2) and bcc(B2) (ordered body centred cubic crystal structure B2, Pearson symbol cP2), as shown in Fig. 2.

Based on the measured chemical composition and XRD analyses, the dendrites belong to fcc(A1) phase. The interdendritic region consists of the ordered bcc(B2) (region 2), net-like disordered bcc(A2) (region 3), net-like fcc(A1) (region 4) and irregularly shaped fcc(A1) (region 5) phases, as shown in Figs. 1c,d.

3.2. Differential thermal analysis and solidification path

Figure 3 shows the typical DTA heating and cooling curves of the as-solidified $Al_{0.5}CoCrFeNi$ alloy. The heating curve (red colour curve) indicates that the melting of the alloy starts at an onset temperature of 1352 °C, continues with a phase transformation at 1368 °C, and the melting is finalized at 1409 °C. The cooling curve (blue colour curve) indicates that the solidification starts at a temperature of 1391 °C, continues with a phase transformation at 1345 °C, and the solidification is finalized at 1335 °C. Figure 4 shows

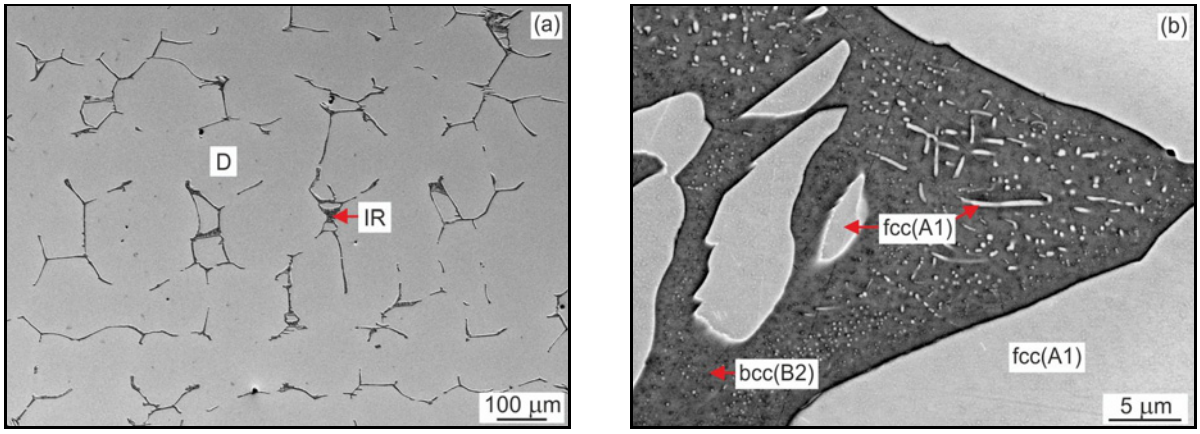

Fig. 5. Microstructure of $Al_{0.5}CoCrFeNi$ alloy solidified at a constant cooling rate of 10 °C min^{-1}: (a) dendritic microstructure of as-solidified sample, LM and (b) microstructure of the interdendritic region, BSE. D – dendrite, IR – interdendritic region.

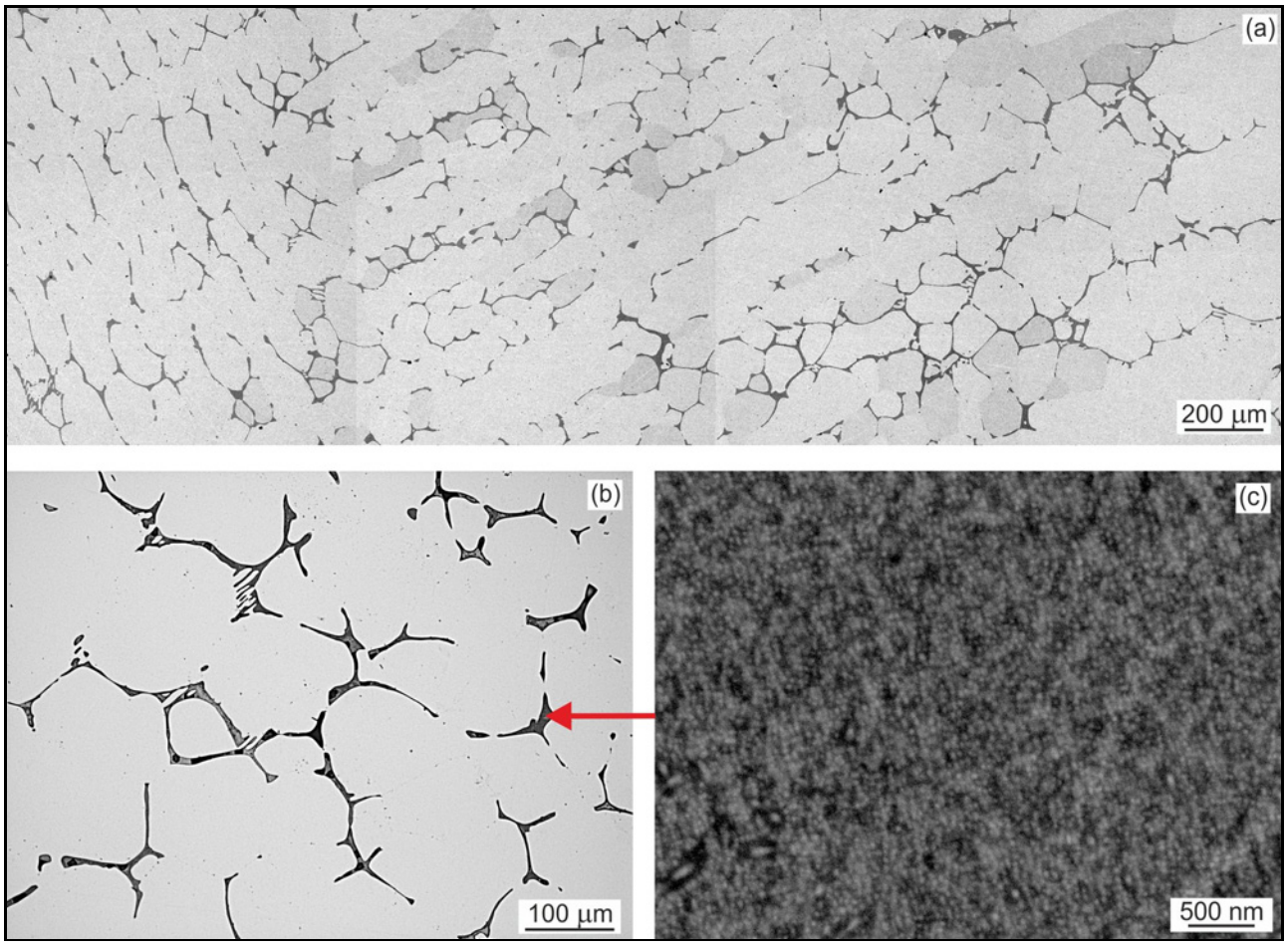

Fig. 6. BSE micrographs showing the effect of solution annealing at 1280 °C for 8 h followed by water quenching on the microstructure of $Al_{0.5}CoCrFeNi$ alloy: (a), (b) preservation of dendritic microstructure during solution annealing; (c) formation of bcc(A2) + bcc(B2) structure in the interdendritic region.

the calculated isopleth for the $Al_xCoCrFeNi$ system reported by Zhang et al. [20]. The chemical composition and experimentally measured phase transformation temperatures of the studied $Al_{0.5}CoCrFeNi$ alloy are marked in the phase diagram by red dashed line and red symbols, respectively. Five independent DTA experiments carried out for the studied alloy lead to an average solidus temperature of $T_S = (1343 \pm 4)$ °C,

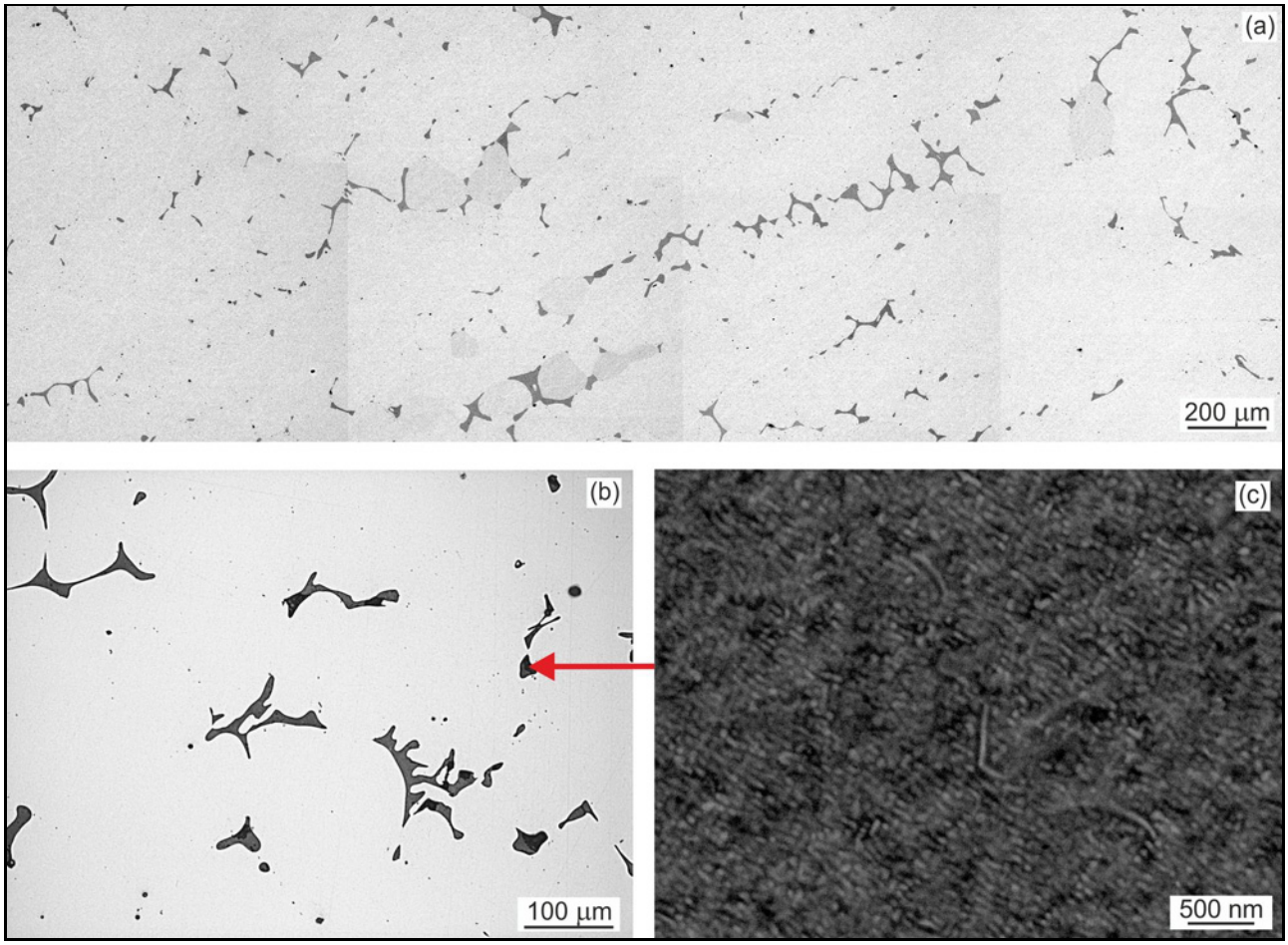

Fig. 7. BSE micrographs showing the effect of solution annealing at 1330 °C for 1 h followed by water quenching of the sample subjected to prior solution annealing at 1280 °C for 8 h on the microstructure of $Al_{0.5}CoCrFeNi$ alloy: (a), (b) partially recrystallized microstructure with remaining coarsened dendrites; (c) formation of bcc(A2) + bcc(B2) structure in the interdendritic region.

a phase transformation during the melting and solidification at a temperature of (1357 ± 4) °C and liquidus temperature of T_L = (1400 ± 4) °C, which correspond very well to those of 1345, 1356, and 1402 °C calculated by Zhang et al. [20], respectively. It should be noted that the experimentally determined phase transformation temperatures differ from those reported by Zhang et al. [19], where T_L and T_S were calculated to be 1380 and 1190 °C, respectively.

The solidification of the studied alloy starts with the formation of fcc(A1) dendrites according to phase transformation sequence L → L + fcc(A1) at a liquidus temperature of 1400 °C. The observed phase transformation temperature of 1357 °C corresponds to transformation sequence L + fcc(A1) → L + fcc(A1) + bcc(B2). The solidification is finalized at a temperature of 1343 °C according to phase transformation sequence L + fcc(A1) + bcc(B2) → fcc(A1) + bcc(B2).

Figure 5 shows the microstructure of $Al_{0.5}CoCrFeNi$ alloy solidified at steady-state growth conditions characterized by a constant cooling rate of 10 °C min^{-1}. The microstructure of the as-solidified alloy consists of fcc(A1) dendrites marked as D (94 vol.%) and interdendritic region marked as IR (6 vol.%), as seen in Fig. 5a. The interdendritic region is composed of bcc(B2) matrix and irregular shaped coarse and fine fcc(A1) particles, as seen in Fig. 5b. The calculated phase diagram also predicts the formation of Cr-rich σ phase (body-centred tetragonal crystal structure) in $Al_{0.5}CoCrFeNi$ alloy at temperatures below 840 °C, as shown in Fig. 4. The formation of σ phase has been confirmed by Butler and Weaver [28] during annealing of $Al_xCoCrFeNi$ alloys at a temperature of 700 °C for 520 h. However, the σ phase can not be identified by XRD analysis in the as-solidified $Al_{0.5}CoCrFeNi$ alloy. The present results indicate that the time required for diffusion-controlled nucleation and growth of σ phase is too short to form a sufficient amount of this phase even at a relatively low constant cooling rate of 10 °C min^{-1}.

3.3. Solution annealing

Figure 6 shows the effect of solution annealing

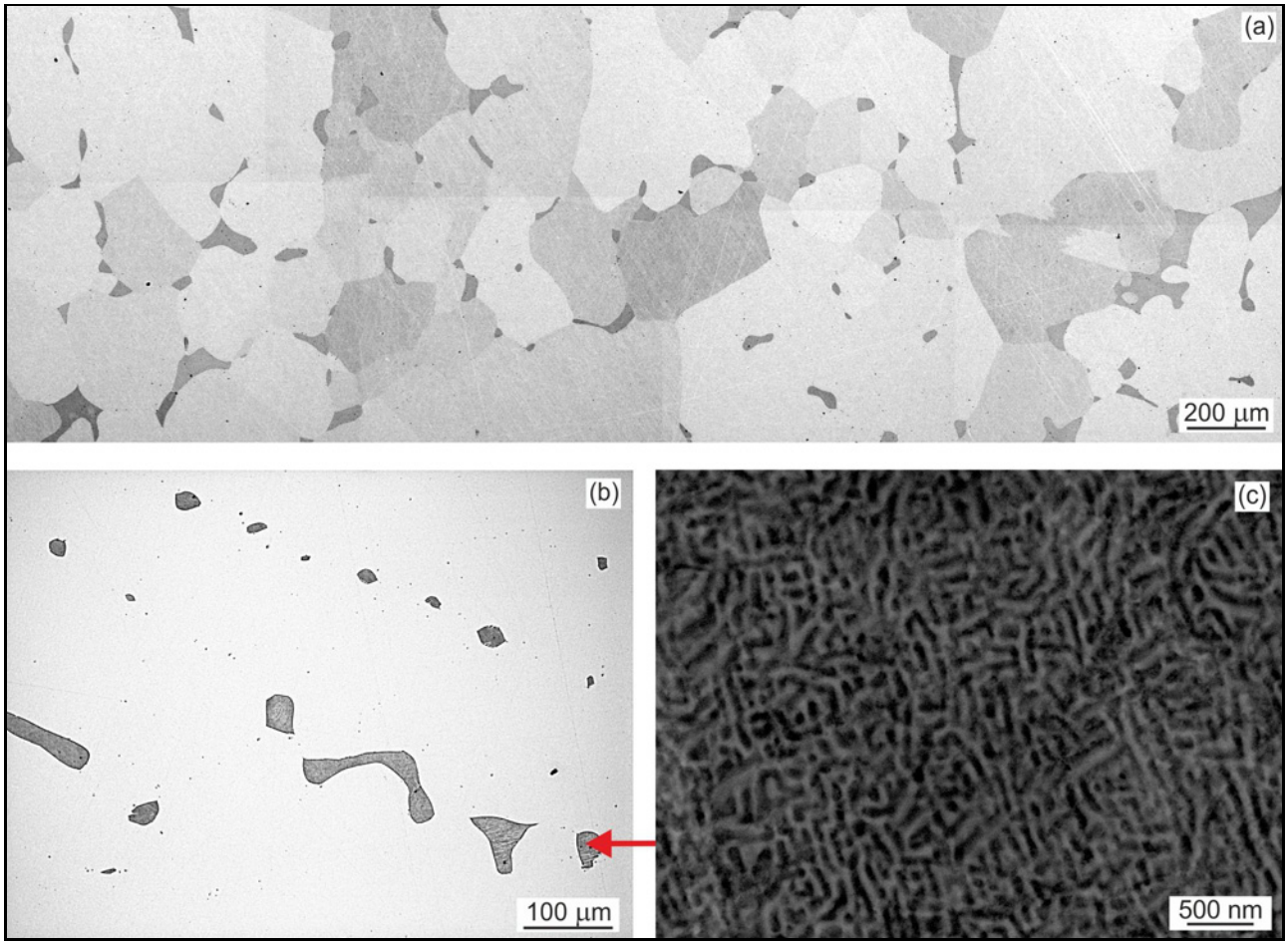

Fig. 8. BSE micrographs showing the effect of solution annealing at 1360 °C for 1 h followed by water quenching of the sample subjected to prior solution annealing at 1280 °C for 8 h on the microstructure of $Al_{0.5}$CoCrFeNi alloy: (a), (b) fully recrystallized fcc(A1) grains; (c) formation of net-like bcc(A2) + bcc(B2) structure in the interdendritic region.

temperature on the microstructure of the as-solidified $Al_{0.5}$CoCrFeNi alloy. The annealing at a temperature of 1280 °C for 8 h followed by water quenching (WQ) preserves the dendritic microstructure, as seen in Figs. 6a,b. The XRD pattern indicates the diffraction peaks of fcc(A1) and bcc(B2) phases, as seen in Fig. 2. This annealing in the fcc(A1) + bcc(B2) phase field leads to a decrease in volume fraction of the interdendritic region to (5.4 ± 0.7) vol.% and dissolution of net-like bcc(A2) phase in the bcc(B2) matrix. The water quenching from the solution annealing temperature leads to the formation of bcc(A2) particles in the bcc(B2) interdendritic region, as shown in Fig. 6c. The formation of cuboidal bcc(A2) particles in bcc(B2) matrix has been reported by Shi et al. [29] for $Al_{0.7}$CoCrFeNi alloy subjected to the solution annealing at 1250 °C for 50 h followed by water quenching. Figure 7 shows the effect of solution annealing at 1330 °C for 1 h followed by water quenching on the microstructure of the sample subjected to prior solution annealing at 1280 °C for 8 h. This solution annealing in fcc(A1) + bcc(B2) phase field affects the dendritic microstructure of the alloy and leads to the formation of a low amount of recrystallized grains, as shown in Figs. 7a,b. The volume fraction of the interdendritic region decreases to (2.9 ± 0.6) vol.%. The water quenching leads to the formation of fine bcc(A2) particles in the interdendritic bcc(B2) phase, as shown in Fig. 7c. Figure 8 shows the effect of solution annealing at 1360 °C for 1 h followed by water quenching on the microstructure of the sample subjected to prior solution annealing at 1280 °C for 8 h. This solution annealing in fcc(A1) + L phase field leads to the formation of fully recrystallized grains with an average grain size of (85 ± 8) µm, as shown in Figs. 8a,b. The volume fraction of the interdendritic region is measured to be (5.0 ± 0.7) vol.%. The water quenching preserves fcc(A1) phase within the recrystallized grains and leads to the formation of net-like bcc(A2) + bcc(B2) structure during quenching of liquid phase formed along some grain boundaries, as shown in Fig. 8c. Wang et al. [30, 31] have reported the formation of high-temperature bcc(A2) phase in the interdendritic region of $Al_{0.5}$CoCrFeNi alloy and

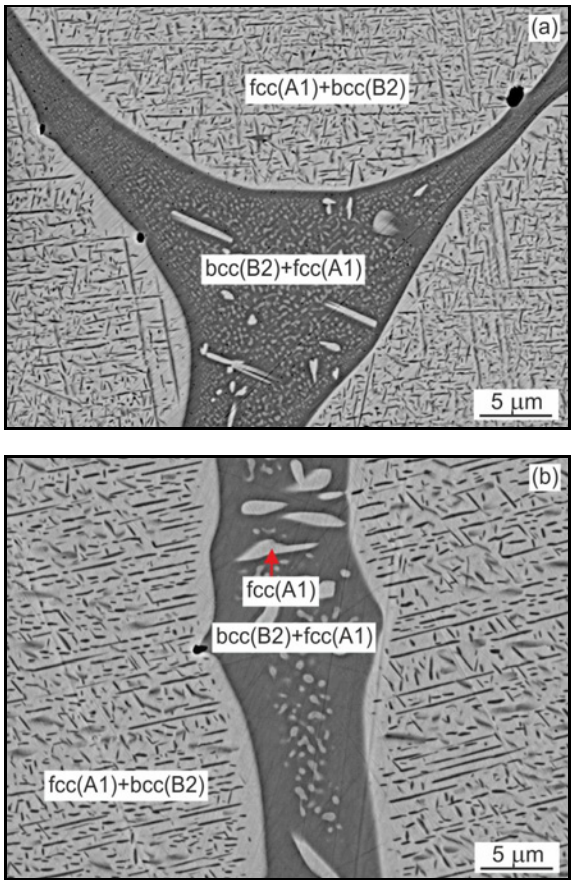

Fig. 9. BSE micrographs showing the microstructure of the heat-treated samples subjected to solution annealing at 1280 °C for 8 h followed by water quenching and ageing at: (a) 800 °C for 25 h; (b) 900 °C for 25 h.

its spinodal decomposition to bcc(A2) + bcc(B2) type of microstructure. However, the experimental results of this work support formation of the ordered bcc(B2) phase during solidification and its spinodal decomposition to bcc(B2) + bcc(A2) phases, which is in agreement with the thermodynamic calculations of Zhang et al. [20], Gwalani et al. [32], and experimental results reported by Rao et al. [14].

3.4. Precipitation hardening

Figure 9 shows the microstructure of $Al_{0.5}$CoCrFeNi alloy after solution annealing at 1280 °C for 8 h, followed by water quenching and ageing. The ageing of the quenched samples at the temperatures of 800 and 900 °C leads to the formation of needle-like precipitates within the fcc(A1) dendrites and fine and coarse precipitates within the bcc(B2) interdendritic region, as shown in Figs. 9a,b. The XRD patterns indicate the diffraction peaks of two phases fcc(A1) and bcc(B2) phases in the samples aged at 800 and 900 °C for 25 h, as seen in Fig. 2. Based on the XRD and

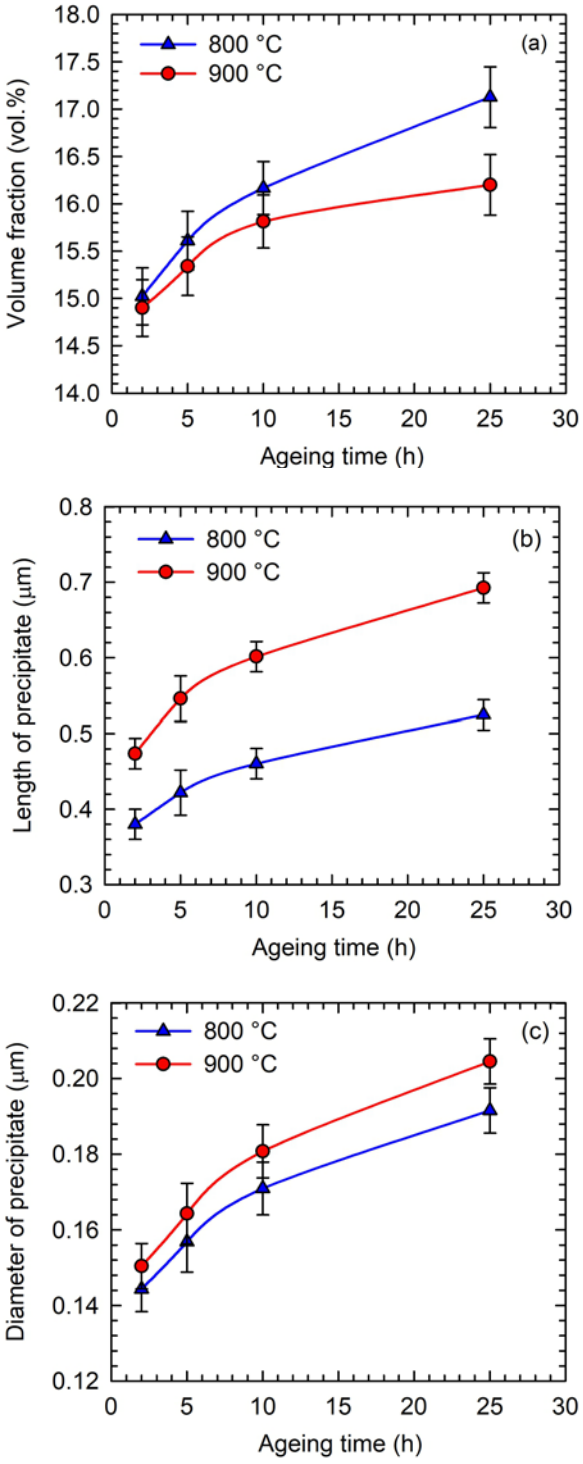

Fig. 10. Effect of ageing time on volume fraction and size of needle-like bcc(B2) precipitates forming in fcc(A1) phase: (a) dependence of volume fraction of precipitates on ageing time; (b) dependence of mean length of precipitates on ageing time; (c) dependence of mean diameter of precipitates on ageing time. The ageing temperatures are indicated in the figures.

EDS analyses, the needle-like precipitates forming in the dendrites belong to the bcc(B2) phase and coarse

and fine precipitates in the bcc(B2) interdendritic region to fcc(A1) phase. According to the phase diagram (Fig. 4) calculated by Zhang et al. [20] and experimental results reported by Butler and Weaver [28], the ageing at temperatures below 840 °C should lead to the formation of σ phase. The thermodynamic calculations of Stryzhyboroda et al. [22] indicate the stability of σ phase up to a temperature of 960 °C. However, the ageing time of 25 h at both ageing temperatures of 800 and 900 °C is too short for the formation of a sufficient amount of σ phase, which can be identified by the XRD or EDS analysis in the present work.

Figure 10 shows the effect of ageing time and ageing temperature on volume fraction, length, and diameter of needle-like bcc(B2) precipitates formed within the fcc(A1) dendrites in the samples subjected to solution annealing at 1280 °C for 8 h followed by water quenching and ageing. The volume fraction of bcc(B2) precipitates increases with increasing ageing time and decreases with increasing ageing temperature, as seen in Fig. 10a. The decrease in the volume fraction of needle-like bcc(B2) precipitates with the increasing ageing temperature is connected with the increasing Al solubility in fcc(A1) phase, as seen in Fig. 4. The mean length and mean diameter of bcc(B2) precipitates increase with increasing ageing time and increasing ageing temperature, as shown in Figs. 10b,c. Aizenshtein et al. [33] have reported that the dominant morphology of bcc(B2) precipitates is needle-like up to a temperature of 1000 °C and changes completely to equiaxed at 1200 °C. The coarsening kinetics of equiaxed bcc(B2) particles can be described by Lifshitz and Slyozov [34] kinetic equation with activation energy for particle coarsening of 187 kJ mol^{-1} [33].

3.5. Vickers microhardness and hardness

Figure 11 shows the dependence of Vickers microhardness of dendrites and Vickers hardness of $Al_{0.5}$CoCrFeNi alloy on the ageing time at the ageing temperatures of 800 and 900 °C. Both the microhardness HV_m and hardness HV increase with increasing ageing time up to 5 h and then decrease at a longer ageing time. The ageing in fcc(A1) + bcc(B2) + σ phase field at an ageing temperature of 800 °C results in significantly higher microhardness and hardness values compared to those of the samples aged in fcc(A1) + bbc(B2) phase field at 900 °C. Assuming precipitation hardening theories reviewed by Ardell [35], the increase of HV_m and HV can be attributed mainly to a higher volume fraction, smaller size and coherency of needle-like bcc(B2) precipitates forming at 800 °C compared to those forming during ageing at 900 °C. It should be noted that the measured Vickers hardness values for the samples aged at 800 °C are higher than those ranging from 245 to 285 reported for as-cast $Al_{0.5}$CoCrFeNi alloy aged at temperatures

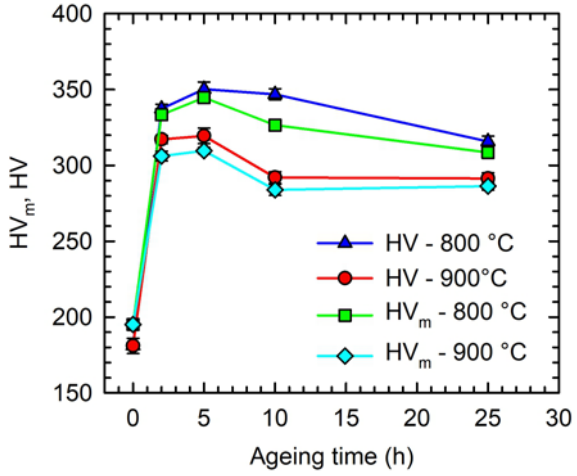

Fig. 11. Dependence of Vickers microhardness HV_m and Vickers hardness HV on ageing time. The ageing temperatures are indicated in the figure.

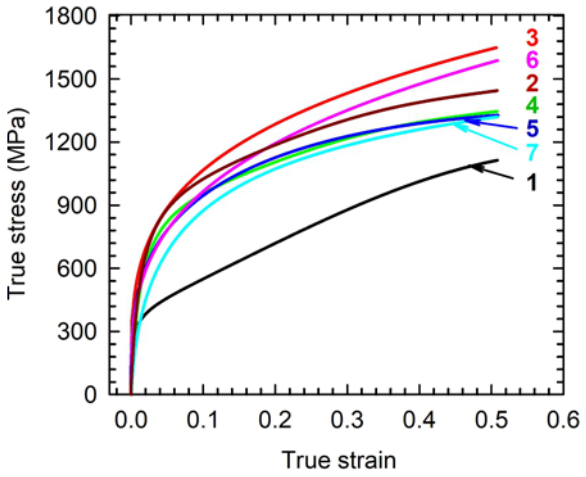

Fig. 12. Examples of compressive true stress–true strain curves for water quenched (WQ) and aged specimens: 1 – WQ, 2 – 800 °C/2 h, 3 – 800 °C/5 h, 4 – 800 °C/25 h, 5 – 900 °C/2 h, 6 – 900 °C/5 h, and 7 – 900 °C/25 h.

ranging from 350 to 950 °C for 24 h [36] or those ranging from 258 to 302 after solution annealing at 1150 °C followed by ageing at 700 °C up to 80 h [32].

3.6. Room temperature compressive behaviour

Figure 12 shows examples of room temperature compressive true stress-true strain curves measured for the specimens subjected to solution annealing at 1280 °C for 8 h followed by water quenching and ageing at the temperatures of 800 and 900 °C for a various time ranging from 2 to 25 h. Figure 13 shows the dependence of room temperature 0.2 % offset compressive yield strength on ageing time. The yield strength

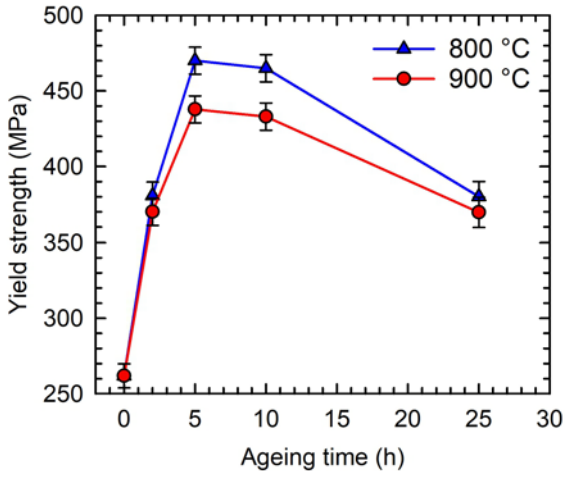

Figure 13. Dependence of 0.2 % offset compressive yield strength on the ageing time. The ageing temperatures are indicated in the figure.

increases with increasing ageing time up to 5 h and then decreases at a longer ageing time at both ageing temperatures of 800 and 900 °C. The ageing at 800 °C results in higher yield strength values compared to those of the specimens aged at 900 °C. According to precipitation hardening theories [35], the higher compressive yield strength of the specimens subjected to ageing at 800 °C can be attributed mainly to a higher volume fraction, smaller size and coherency of needle-like bcc(B2) precipitates forming in fcc(A1) matrix compared to those of the specimens aged at 900 °C.

The compressive curves show a clear work hardening during deformation up to a true strain of 0.5. The work hardening behaviour can be characterized by work hardening rate (WHR), defined as:

$$\mathrm{WHR} = \frac{\partial \sigma_\mathrm{t}}{\partial \varepsilon_\mathrm{t}}, \tag{1}$$

where σ_t is the true stress and ε_t is the true strain. Three different regions can be well identified on the WHR curves, as illustrated for the compression specimen aged at 800 °C/5 h in Fig. 14. Region I is characterized by a fast decrease of the WHR up to a true strain of 0.057 or up to true stress of 1168 MPa, as seen in Figs. 14a,b. Region II observed at a true strain ranging from 0.057 to 0.382 or at true stress ranging from 1180 to 1566 MPa is characterized by a gradual decrease in WHR with increasing true strain or true stress. The high WHR measured in region II is controlled by an increase of dislocation density and mechanical twinning in the fcc(A1) matrix [37, 38]. The fast decrease of the WHR in region III at a true strain or true stress higher than 0.382 or 1566 MPa, respectively, indicates an intensive softening of the $Al_{0.5}CoCrFeNi$ alloy. Figure 15 shows a longitudinal section of the specimen

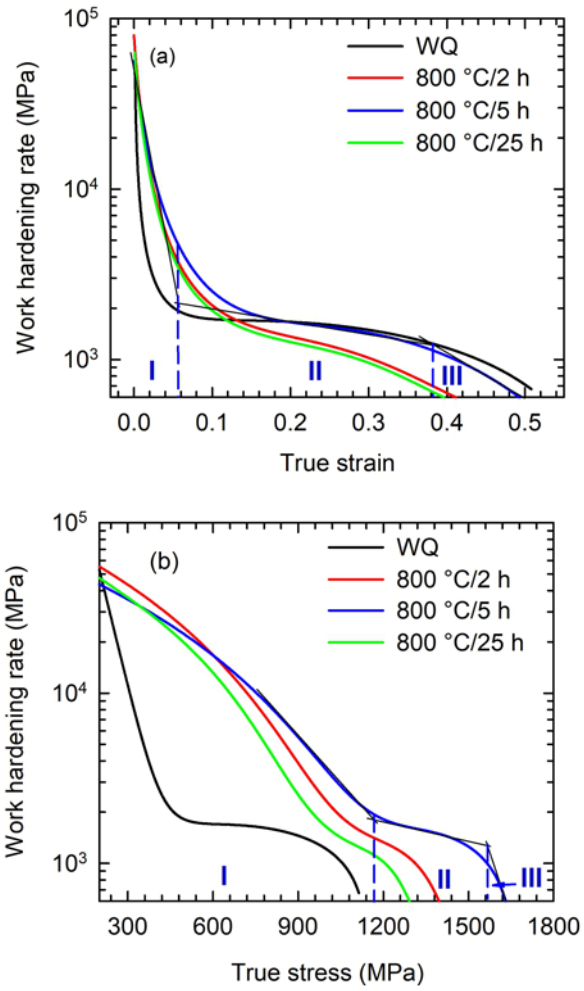

Fig. 14. (a) Dependence of work hardening rate on true strain and (b) dependence of work hardening rate on true stress. The heat treatment conditions of the compression specimens are indicated in the figures.

aged at 800 °C/5 h after compressive deformation to a true strain of 0.5. The contour curve of the deformed specimen contains multiple visible protuberances, which can be related to the individual columnar grains, as seen in Fig. 15a. Similar formation of protuberances on deformed surfaces of compression specimens was reported by Štamborská and Lapin [10] for $Co_{24}Cr_{19}Fe_{24}Ni_{19}Al_8(Ti,Si,C)_6$ (at.%) alloy with anisotropic as-cast microstructure and related to deformation behaviour of individual columnar grains during compression. Figure 15b indicates that the fast decrease of WHR in region III is connected with the initiation and propagation of cracks in the barrelled region of the compression specimen. It should be noted that the initiation and propagation of cracks have not been observed in the WQ compression specimens, which showed a significantly lower compressive yield strength and moderate WHR compared to those of the precipitation-hardened ones.

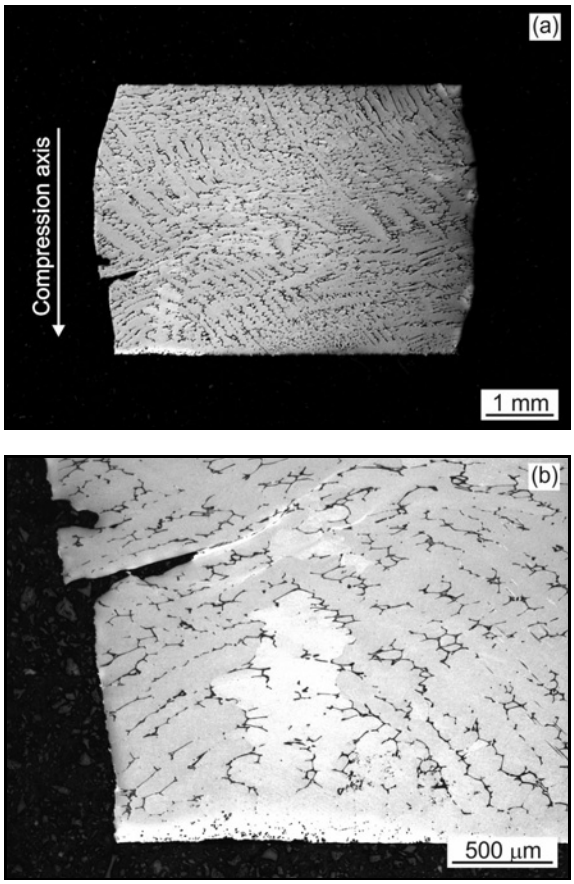

Fig. 15. LM micrographs showing a longitudinal section of the specimen aged at 800 °C/5 h after compressive deformation to a true strain of 0.5 at room temperature: (a) barrelled shape of compression specimen with protuberances and (b) propagation of a crack in the direction parallel to columnar dendrites.

Figures 13 and 14 indicate that a low yield strength, moderate strain hardening rate, and good ductility at room temperature of the studied $Al_{0.5}$CoCrFeNi alloy can be achieved by solid solution annealing followed by water quenching (WQ), which is considered to be beneficial to some cold working processes such as cold rolling. High yield strength and high WHR required for high-temperature structural applications can be achieved by appropriate heat treatments consisting of solution annealing, quenching, and precipitation hardening.

4. Conclusions

The effect of heat treatments on microstructure and mechanical properties of $Al_{0.5}$CoCrFeNi complex concentrated alloy was studied. The achieved results can be summarized as follows:

1. The dendritic microstructure of the as-solidified alloy consists of fcc(A1) dendrites and an interdendritic region composed of bcc(B2), bcc(A2) and fcc(A1) phases. The solidification path and phase transformation temperatures determined experimentally at steady-state growth conditions correspond to some recent thermodynamical calculations.

2. The increase of solid solution annealing temperature from 1280 to 1360 °C leads to full recrystallization of as-solidified dendritic microstructure, formation of equiaxed grains, and decrease in volume fraction of the interdendritic region.

3. The solid solution annealing at 1280 °C followed by water quenching and ageing at 800 and 900 °C leads to the precipitation of needle-like bcc(B2) particles in fcc(A1) dendrites and the formation of the interdendritic region composed of bcc(B2) and fcc(A1) phases. The volume fraction of bcc(B2) precipitates increases with increasing ageing time and decreasing ageing temperature. The length and diameter of needle-like precipitates increase with increasing ageing time and ageing temperature.

4. Solid solution annealing followed by water quenching of as-solidified alloy results in low compressive yield strength, moderate strain hardening rate, and good ductility at room temperature. Vickers microhardness, Vickers hardness, and room temperature compressive yield strength of the precipitation hardened alloy increase with decreasing ageing temperature and increasing ageing time up to 5 h and then decrease at a longer ageing time up to 25 h.

Acknowledgement

This research was funded by the Slovak Grant Agency for Science under the contract VEGA 2/0074/19.

References

[1] D. B. Miracle, O. N. Senkov, A critical review of high entropy alloys and related concepts, Acta Mater. 122 (2017) 448–511. doi:10.1016/j.actamat.2016.08.081

[2] S. Gorsse, D. B. Miracle, O. N. Senkov, Mapping the world of complex concentrated alloys, Acta Mater. 135 (2017) 177–187. doi:10.1016/j.actamat.2017.06.027

[3] W. Steurer, Single-phase high-entropy alloys – A critical update, Mater. Charact. 162 (2020) 110179. doi:10.1016/j.matchar.2020.110179

[4] A. O. Soto, A. S. Salgado, E. B. Niño, Thermodynamic analysis of high entropy alloys and their mechanical behavior in high and low-temperature conditions with a microstructural approach – A review, Intermetallics 124 (2020) 106850. doi:10.1016/j.intermet.2020.106850

[5] Y. Ma, B. Jiang, C. Li, Q. Wang, C. Dong, P.K. Liaw, F. Xu, L. Sun, The BCC/B2 morphologies in Al_xNiCoFeCr high-entropy alloys, Metals (Basel) 7 (2017) 1–12. doi:10.3390/met7020057

[6] J. W. Yeh, S. K. Chen, S. J. Lin, J. Y. Gan, T. S. Chin, T. T. Shun, C. H. Tsau, S. Y. Chang, Nanostructured

high-entropy alloys with multiple principal elements: Novel alloy design concepts and outcomes, Adv. Eng. Mater. 6 (2004) 299–303. doi:10.1002/adem.200300567

[7] J. W. Yeh, Alloy design strategies and future trends in high-entropy alloys, JOM 65 (2013) 1759–1771. doi:10.1007/s11837-013-0761-6

[8] J. W. Yeh, S. K. Chen, J. Y. Gan, S. J. Lin, T. S. Chin, Formation of simple crystal structures in Cu-Co-Ni--Cr-Al-Fe-Ti-V alloys with multiprincipal metallic elements, Metall. Mater. Trans. A 35 (2010) 2533–2536. doi:10.1007/s11661-006-0234-4

[9] B. Cantor, Progress in materials science multicomponent high-entropy Cantor alloys, Prog. Mater. Sci. (2020) 100754. doi:10.1016/j.pmatsci.2020.100754

[10] M. Štamborská, J. Lapin, Effect of anisotropic microstructure on high-temperature compression deformation of CoCrFeNi based complex concentrated alloy, Kovove Mater. 55 (2017) 369–378. doi:10.4149/km_2017_6_369

[11] W. R. Wang, W. L. Wang, S. C. Wang, Y. C. Tsai, C. H. Lai, J. W. Yeh, Effects of Al addition on the microstructure and mechanical property of Al_xCoCrFeNi high-entropy alloys, Intermetallics 26 (2012) 44–51. doi:10.1016/j.intermet.2012.03.005

[12] J. Joseph, N. Stanford, P. Hodgson, D. M. Fabijanic, Understanding the mechanical behaviour and the large strength/ductility differences between FCC and BCC Al_xCoCrFeNi high entropy alloys, J. Alloys Compd. 726 (2017) 885–895. doi:10.1016/j.jallcom.2017.08.067

[13] Y. Lv, R. Hu, Z. Yao, J. Chen, D. Xu, Y. Liu, X. Fan, Cooling rate effect on microstructure and mechanical properties of Al_xCoCrFeNi high entropy alloys, Mater. Des. 132 (2017) 392–399. doi:10.1016/j.matdes.2017.07.008

[14] J. C. Rao, H. Y. Diao, V. Ocelík, D. Vainchtein, C. Zhang, C. Kuo, Z. Tang, W. Guo, J. D. Poplawsky, Y. Zhou, P. K. Liaw, J. T. M. De Hosson, Secondary phases in Al_xCoCrFeNi high-entropy alloys: An in-situ TEM heating study and thermodynamic appraisal, Acta Mater. 131 (2017) 206–220. doi:10.1016/j.actamat.2017.03.066

[15] J. C. Rao, D. Vainchtein, Z. Tang, P. K. Liaw, The fcc-bcc crystallographic orientation relationship in Al_xCoCrFeNi high-entropy alloys, Mater. Lett. 176 (2016) 29–32. doi:10.1016/j.matlet.2016.04.086

[16] Y. F. Kao, T. J. Chen, S. K. Chen, J. W. Yeh, Microstructure and mechanical property of as-cast, -homogenized, and -deformed Al_xCoCrFeNi ($0 \leq x \leq 2$) high-entropy alloys, J. Alloys Compd. 488 (2009) 57–64. doi:10.1016/j.jallcom.2009.08.090

[17] W. R. Wang, W. L. Wang, S. C. Wang, Y. C. Tsai, C. H. Lai, J. W. Yeh, Effects of Al addition on the microstructure and mechanical property of Al_xCoCrFeNi high-entropy alloys, Intermetallics 26 (2012) 44–51. doi:10.1016/j.intermet.2012.03.005

[18] T. T. Shun, Y. C. Du, Microstructure and tensile behaviors of FCC $Al_{0.3}$CoCrFeNi high entropy alloy, J. Alloys Compd. 479 (2009) 157–160. doi:10.1016/j.jallcom.2008.12.088

[19] C. Zhang, F. Zhang, S. Chen, W. Cao, Computational thermodynamics aided high-entropy alloy design, JOM 64 (2012) 839–845. doi:10.1007/s11837-012-0365-6

[20] C. Zhang, F. Zhang, H. Diao, M. C. Gao, Z. Tang, J. D. Poplawsky, P. K. Liaw, Understanding phase stability of Al-Co-Cr-Fe-Ni high entropy alloys, Mater. Des. 109 (2016) 425–433. doi:10.1016/j.matdes.2016.07.073

[21] J. E. Saal, I. S. Berglund, J. T. Sebastian, P. K. Liaw, G. B. Olson, Equilibrium high entropy alloy phase stability from experiments and thermodynamic modeling, Scr. Mater. 146 (2018) 5–8. doi:10.1016/j.scriptamat.2017.10.027

[22] O. Stryzhyboroda, V. T. Witusiewicz, S. Gein, D. Röhrens, U. Hecht, Phase equilibria in the Al-Co--Cr-Fe-Ni high entropy alloy system: Thermodynamic description and experimental study, Front. Mater. 7 (2020) 1–13. doi:10.3389/fmats.2020.00270

[23] A. D. Pogrebnjak, A. A. Bagdasaryan, I. V Yakushchenko, V. M. Beresnev, The structure and properties of high-entropy alloys and nitride coatings based on them, Russ. Chem. Rev. 83 (2014) 1027–1061. doi:10.1070/rcr4407

[24] A. Klimová, J. Lapin, Effects of C and N additions on primary MAX phase particles in intermetallic Ti-Al--Nb-Mo matrix in-situ composites prepared by vacuum induction melting, Kovove Mater. 57 (2019) 151–157. doi:10.4149/km_2019_3_151

[25] A. Klimová, J. Lapin, Effect of Al content on microstructure of Ti-Al-Nb-C-Mo composites reinforced with carbide particles, Kovove Mater. 57 (2019) 377–387. doi:10.4149/km_2019_6_377

[26] J. Lapin, A. Klimová, Vacuum induction melting and casting of TiAl-based matrix in-situ composites reinforced by carbide particles using graphite crucibles and moulds, Vacuum 169 (2019) 108930. doi:10.1016/j.vacuum.2019.108930

[27] K. Kamyshnykova, J. Lapin, Vacuum induction melting and solidification of TiAl-based alloy in graphite crucibles, Vacuum 154 (2018) 218–226. doi:10.1016/j.vacuum.2018.05.017

[28] T. M. Butler, M. L. Weaver, Investigation of the phase stabilities in AlNiCoCrFe high entropy alloys, J. Alloys Compd. 691 (2017) 119–129. doi:10.1016/j.jallcom.2016.08.121

[29] Y. Shi, L. Collins, R. Feng, C. Zhang, N. Balke, P. K. Liaw, B. Yang, Homogenization of Al_xCoCrFeNi high--entropy alloys with improved corrosion resistance, Corros. Sci. 133 (2018) 120–131. doi:10.1016/j.corsci.2018.01.030

[30] W.-R. Wang, W.-L. Wang, S.-C. Wang, Y.-C. Tsai, C.-H. Lai, J.-W. Yeh, Effects of Al addition on the microstructure and mechanical property of Al_xCoCrFeNi high-entropy alloys, Intermetallics 26 (2012) 44–51. doi:10.1016/j.intermet.2012.03.005

[31] W. R. Wang, W. L. Wang, J. W. Yeh, Phases, microstructure and mechanical properties of Al_xCoCrFeNi high-entropy alloys at elevated temperatures, J. Alloys Compd. 589 (2014) 143–152. doi:10.1016/j.jallcom.2013.11.084

[32] B. Gwalani, T. Torgerson, S. Dasari, A. Jagetia, M. S. K. K. Y. Nartu, S. Gangireddy, M. Pole, T. Wang, T. W. Scharf, R. Banerjee, Influence of fine-scale B2 precipitation on dynamic compression and wear properties in hypo-eutectic $Al_{0.5}$CoCrFeNi high--entropy alloy, J. Alloys Compd. 853 (2021) 157126. doi:10.1016/j.jallcom.2020.157126

[33] M. Aizenshtein, E. Strumza, E. Brosh, S. Hayun, Microstructure, kinetics and thermodynamics of HEA

$Al_{0.5}$CoCrFeNi at $T \geq 800\,°C$, Mater. Charact. 171 (2021) 1–9. doi:10.1016/j.matchar.2020.110738

[34] I. M. Lifshitz, V. V. Slyozov, The kinetics of precipitation from supersaturated solid solutions, J. Phys. Chem. Solids 19 (1961) 35–50. doi:10.1016/0022-3697(61)90054-3

[35] A. J. Ardell, Precipitation hardening, Metall. Mater. Trans. A 16 (1985) 2131–2165. doi:10.1007/BF02670416

[36] C. M. Lin, H. L. Tsai, Evolution of microstructure, hardness, and corrosion properties of high-entropy $Al_{0.5}$CoCrFeNi alloy, Intermetallics 19 (2011) 288–294. doi:10.1016/j.intermet.2010.10.008

[37] M. Bönisch, Y. Wu, H. Sehitoglu, Twinning-induced strain hardening in dual-phase FeCoCrNi$Al_{0.5}$ at room and cryogenic temperature, Sci. Rep. 8 (2018) 1–9. doi:10.1038/s41598-018-28784-1

[38] J. Li, H. Yang, W. Y. Wang, H. Kou, J. Wang, Thermal-mechanical processing and strengthen in Al_xCoCrFeNi high-entropy alloys, Front. Mater. 7 (2021) 1–17. doi:10.3389/fmats.2020.585602